

**FPMC2013-4481**

**DESIGN AND PRECISION CONTROL OF AN MR-COMPATIBLE FLEXIBLE FLUIDIC ACTUATOR**

**David B. Comber**

Department of Mechanical Engineering  
Vanderbilt University  
Nashville, TN 37235  
david.b.comber@vanderbilt.edu

**Eric J. Barth**

Department of Mechanical Engineering  
Vanderbilt University  
Nashville, TN 37235  
eric.j.barth@vanderbilt.edu

**Robert J. Webster III**

Department of Mechanical Engineering  
Vanderbilt University  
Nashville, TN 37235  
robert.webster@vanderbilt.edu

**Jonathon E. Slightam**

Rapid Prototyping Research  
Milwaukee School of Engineering  
Milwaukee, WI 53202  
slightamj@msoe.edu

**Vito R. Gervasi**

Rapid Prototyping Research  
Milwaukee School of Engineering  
Milwaukee, WI 53202  
gervasi@msoe.edu

**ABSTRACT**

*Magnetic resonance imaging (MRI) offers many benefits to image-guided interventions, including excellent soft tissue distinction, little to no repositioning of the patient, and zero radiation exposure. The closed, narrow bore of a high field MRI scanner limits clinician access to the patient, such that an MR-compatible robot is essentially required for many potential interventions. A robotic system of this kind could additionally provide the clinician increased accuracy and more degrees of freedom within the minimally invasive context. Fluid power is an excellent type of actuation to use inside the MRI scanner, as such actuators can be designed free of magnetic and electrical components. However, there are no fluid power actuators readily available that are suitable for use in the operating room. This paper reports a compact, intrinsically safe, sterilizable fluid power actuator. Using additive manufacturing processes, the actuator was printed in a single build. Thus, it is composed of several integrated parts in a compact design. Employing an inchworm-like behavior, the linear actuator can advance or retract a needle or mechanism rod in discrete steps; thus the device is intrinsically safe. The actuator is fluid agnostic, but a pneumatic prototype is presented here with initial testing results. For the pneumatic case, sub-step*

*positioning control has been tested using a nonlinear, model-based controller, and the mean steady-state error was 0.025 mm. Thus this type of actuator appears to be promising solution for use in MRI-guided interventions.*

**INTRODUCTION**

Medical robotic systems for image-guided interventions require safe, sterilizable (or disposable), precision actuators. Imaging modalities like computed tomography (CT) and magnetic resonance imaging (MRI) impose further limitations on the design of such actuators. It is desirable for the robot and its actuators to be transparent to the imager and to not produce artifacts, noise or distortion in the images. Thus, actuator design is restricted to materials and principles of operation that are compatible with the imaging environment. Together with the requirements for safety, sterilizability and precision control, these restrictions present a challenging design problem.

Over the past 20 years, numerous custom MR-compatible actuators have been reported in the literature. Due to the high strength magnetic field of the MR imager, these actuators cannot contain ferromagnetic materials. Pneumatic actuation has been commonly employed because the working principle

does not rely on electromagnetism. Thus, these actuators can be constructed solely from diamagnetic materials. Stoianovici et al. reported a pneumatic step motor, PneuStep, which consists of three pulsing diaphragms that rotate a harmonic gear drive [1]. Using several of these motors to actuate an MRI-guided robot, Muntener et al. demonstrated transperineal prostate brachytherapy in a canine model [2]. Similarly, using reciprocating piston-cylinders to drive a ratcheting stepper mechanism, Zemiti et al. developed a CT- and MR-compatible needle puncture robot for abdominal procedures [3]. Using both hydraulic and pneumatic piston-cylinders, van den Bosch et al. reported a momentum-based needle tapping device for prostate interventions [4].

Departing from the stepping mechanism approach, INNOMOTION, one of the few commercially available MRI-guided robotic systems, addressed the need for safety by custom designing pneumatic piston-cylinders to exhibit high dynamic and low static friction [5]. Tokuda et al. demonstrated a needle positioning device employing four pneumatic piston-cylinders, opting for manual needle insertion by the radiologist for safety [6]. The aforementioned research efforts employing pneumatic actuation have targeted MRI-guided interventions solely in the abdomen and lower torso, while this work aims to develop MR-compatible pneumatic approaches towards new intracranial interventions.

Other forms of actuation, in particular piezoelectrics, have been employed in a variety of anatomy-specific MR-compatible robots, including several for neurosurgical procedures [7-9]. While piezoelectrics offer precision, safe and non-backdrivable actuation, many researchers have reported its high voltage drive to substantially reduce the signal-to-noise (SNR) ratio of the MR imager, precluding the ability to servo the robot motors while simultaneously acquiring images [8]. However, by using low-noise, non-harmonic piezoelectric motors as well as replacing the commercial motor driver boards with custom, low-noise drivers, Su et al. recently achieved a low SNR of 2% with motors servoing at full speed [10]. Although piezoelectric actuators can be a viable solution for MR-compatible robots, a lower-cost, customizable actuator that does not require extreme care in the design and shielding of drive electronics is desirable.

Flexible fluidic actuators (FFA's) have also been used in MR-compatible robotic systems, such as a needle positioning device actuated by 12 pneumatic muscles [11]. More broadly, a variety of medical instruments have employed FFA's. Ikuta et al. reported a multi-degrees-of-freedom (DOF) active catheter actuated by miniature saline bellows, which were additively manufactured by stereolithography [12]. Similarly, Haga et al. developed a hydraulic suction active catheter and guide wire for intravascular diagnosis and therapy [13]. Further review of fluidic-based actuators, manipulators and end effectors can be found in [14].

While pneumatic FFA's meet the gold standard of MRI-compatibility, they do require a careful treatment of the highly nonlinear pressure and mass flow dynamics in order to achieve

precision control, as well as an accurate modeling of the bellows/muscle behavior. Reynolds et al. showed the muscle is well described as a parallel arrangement of a spring element, damper element and contractile element [15]. Slightam and Gervasi reported viscoelastic modeling and experimental characterization of FFA's manufactured by selective laser sintering (SLS) [16]. Richer and Hurmuzlu introduced a nonlinear mathematical model for the pneumatic servo dynamics and demonstrated substantial improvements in bandwidth and force capabilities using sliding mode control [17-18]. Zhu and Barth achieved sub-millimeter positioning accuracy of 0.05 mm steady-state error using a composite adaptive and sliding mode force controller for an industrial robot [19]. Comber et al. reported sliding mode control of piston-cylinder actuated mechanisms on an MR-compatible active cannula robot, with mean steady-state errors of 0.032 mm and 0.447 degrees, resulting in a mean open-loop cannula tip error of 1.18 mm [20-21].

This paper reports a one degree-of-freedom linear stepping device for safe insertion and retraction of a needle. The device is suitable for use in a variety of MRI-guided interventions. The major contributions of this FFA prototype are several. By integrating additional mechanisms with the actuator during manufacture, the device achieves a compact but simple design. This integrated functionality is uniquely realizable with additive manufacturing technologies like SLS. Additionally, the SLS process enables hermetic sealing of the device for sterilizability. Furthermore, due to the inherent safety of the stepping mechanism, this FFA device has the potential to streamline needle placement if used in an automated manner.

## ACTUATOR DESIGN

In the early conceptual stage of the FFA design, important design requirements were identified. Given its intended use for MRI-guided interventions, the device was required to be safe, such that any malfunction of the pneumatic servo control would not endanger the patient. The MRI environment dictated that the device be non-magnetic with minimal or no electronics in the scanner. A hermetically sealed device was desirable for a clean and sterile setup that would isolate the fluid circuit from the surgical field. To enable access to the patient and integration with surgical workflow, device compactness was an additional general objective.

Several conceptual designs were conceived and evaluated with respect to these design criteria. The best-suited concept was step-like movement of the needle by means of a linear, toroidal bellows. The toroid configuration provides a compact, low-profile design in which a high power-to-size ratio is realizable. The needle feeds through the central axis of the toroidal bellows. This symmetrical configuration also sidesteps issues (e.g. binding friction, unwanted angular deflections) that commonly occur for off-axis loadings.

The FFA provides bi-directional linear actuation to the needle in discrete increments, similar to locomotion of an

inchworm. The needle is grasped by a pinching mechanism, which consists of two flat diaphragms that, upon inflation, sandwich a short section of silicone tubing against the needle, providing sufficient friction to grasp it. While the needle is grasped, inflation and deflation of the toroidal bellows provides bi-directional linear displacement of the needle. A photograph of the FFA prototype is shown in Fig. 1, and its footprint is 3.75 inches long by 1.75 inches diameter.

A single step to cause linear motion in one direction consists of the following sequential functions: a. grasp needle, b. inflate bellows, c. release grasp, and d. deflate bellows. A single step to cause linear motion in the opposing direction consists of the following sequential functions: a. inflate bellows, b. grasp needle, c. deflate bellows, and d. release grasp. Whenever the pinching mechanism has released its grasp on the needle, a needle guide prevents the needle from undergoing any unwanted movement that could be caused by gravitational or other external forces. The needle guide is simply two close fit holes at opposite ends of the FFA housing. This functionality can be likened to the rubber grommet inside a mechanical pencil that holds the graphite stationary while the stepping mechanism resets.

The toroidal bellows and pinching mechanism are hermetically sealed, a desirable quality for maintaining a sterile field for surgery. Hermetic sealing prevents contaminants such as blood or cerebrospinal fluid from entering the fluid circuit, which includes the control valves, transmission lines, pressure sensors and reservoirs employed to control the stepper motor.

### Toroidal Bellows Design

In designing the toroidal bellows, an operating pressure range of 584 to 928 kPa was identified as characteristic for instrument air supplies in hospitals. Based on prior work with active cannula robots, a maximum actuator force of 45 N was targeted [20].

The toroid geometry of the bellows presents an interesting mechanical design problem. The connecting channel from one bellows convolution to the next is not located at the central axis

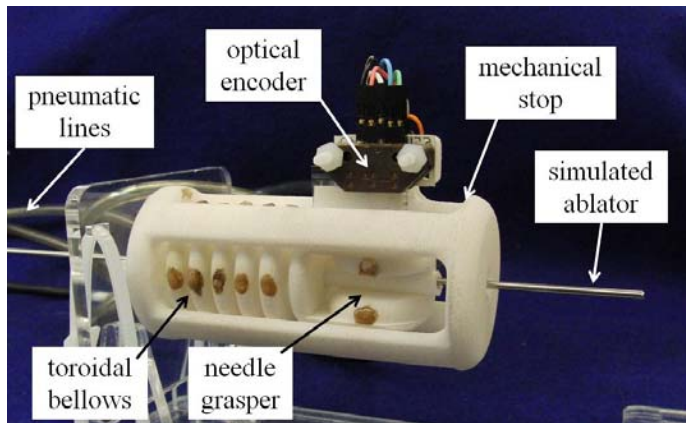


FIG 1. PHOTOGRAPH OF THE FFA PROTOTYPE

of the bellows. Thus the channel is not of the usual cylindrical shape, but rather it is configured like a ring and is located at a distance  $r_2$  from the central axis, as shown in Fig. 2. Due to this configuration the bellows exhibits a near linear behavior, much like a flat diaphragm with rigid center for increased stiffness, and this behavior is desirable for better controllability. However, the toroid design adds complexity to the derivation of expressions for the cross-sectional area  $A$  and stiffness  $k$ .

In choosing the radius  $r_2$ , an important consideration was to equalize the stresses seen at the two extremes of the bellows convolution, namely at  $r_i$  and  $r_o$ . This was accomplished by ensuring the inner and outer annular areas,  $A_i$  and  $A_o$ , were equal. These areas are given by Eqs. (1) and (2).

$$A_i = \pi(r_2 - \frac{1}{2}b_o)^2 - \pi r_i^2 \tag{1}$$

$$A_o = \pi r_o^2 - \pi(r_2 + \frac{1}{2}b_o)^2 \tag{2}$$

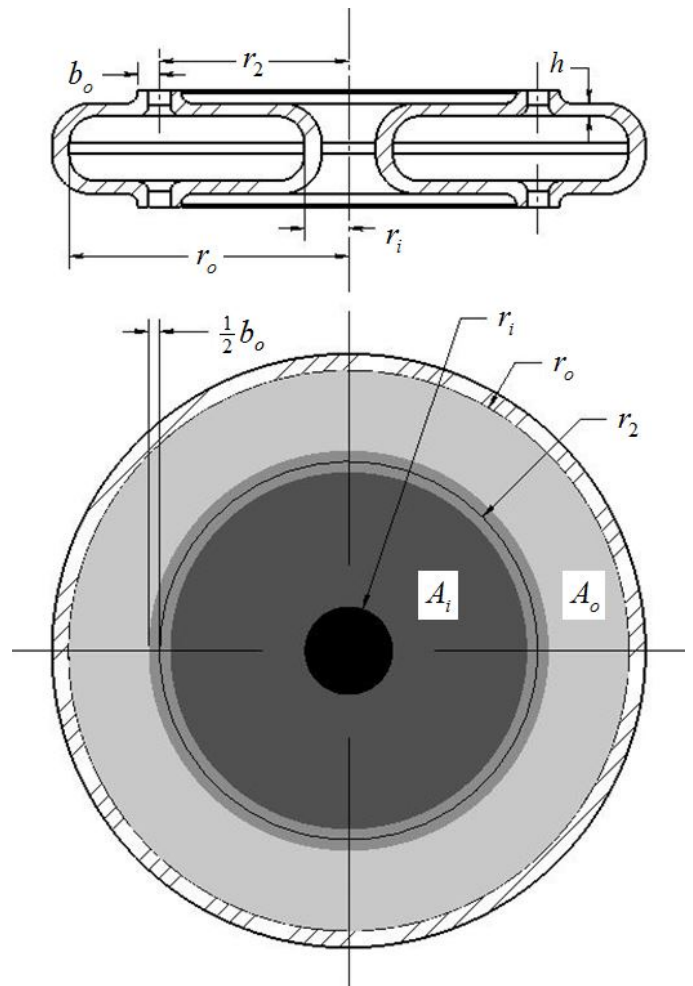


FIG 2. ANNULAR AREAS OF TOROID CONFIGURATION

The actual areas for the outer and inner annular regions are defined by the toroid outer radius  $r_o$ , the toroid inner radius  $r_i$ , and the radial location and thickness of the bellows convolution connecting ring,  $r_2$  and  $b_o$ , respectively. An appropriate choice for  $r_2$  is obtained by setting Eqs. (1) and (2) equal to one another and solving for  $r_2$ , as described by Eq. (3).

$$r_2 = \frac{1}{2} \sqrt{2r_i^2 + 2r_o^2 - b_o^2} \quad (3)$$

To derive expressions for  $A$  and  $k$ , the toroid configuration was assumed to behave like two superimposed flat diaphragms with rigid center (as shown in Fig. 3), one for each of the areas  $A_i$  and  $A_o$ . This superposition requires an effective pressure  $P_{eff}$  for each of the two areas, and this relationship for the outer annular area is determined from Eqs. (2), (4) and (5).

$$P_{o,eff} = \frac{A_o}{A_{o,eff}} P \quad (4)$$

$$A_{o,eff} = \pi r_o^2 \quad (5)$$

Similarly, for the inner annular region, the effective pressure is given by Eqs. (1), (6) and (7).

$$P_{i,eff} = \frac{A_i}{A_{i,eff}} P \quad (6)$$

$$A_{i,eff} = \pi \left( r_2 - \frac{1}{2} b_o \right)^2 \quad (7)$$

Determining the effective pressure acting on the superimposed diaphragms with rigid centers allows for the analysis of bellows deflection, based on various sets of design parameter values—membrane thickness and deflection,  $h$  and  $y_0$ . Optimal values for these parameters were found to match the desired step size or stroke length for the actuator. In the deflection analysis,  $y_0$  is equivalent for both the inner and outer annular regions, and it is sufficient to only arbitrarily analyze either region. The deflection of the rigid-center diaphragm is given by Eq. (9), and  $h$  is adjusted to meet the design requirements.

$$y_0 = A_p \left( \frac{P_{eff} a^4}{Eh^3} \right) \quad (9)$$

The stiffness coefficient  $A_p$  accounts for the increased rigidity of the diaphragm due to the now rigid center, and it is defined by Poisson's ratio  $\mu$  and the solidity ratio  $b/a$ , where  $b$  is the rigid center radius and  $a$  is the flat diaphragm radius, as described by Eq. (10). Equations (9)-(12) are taken from [22].

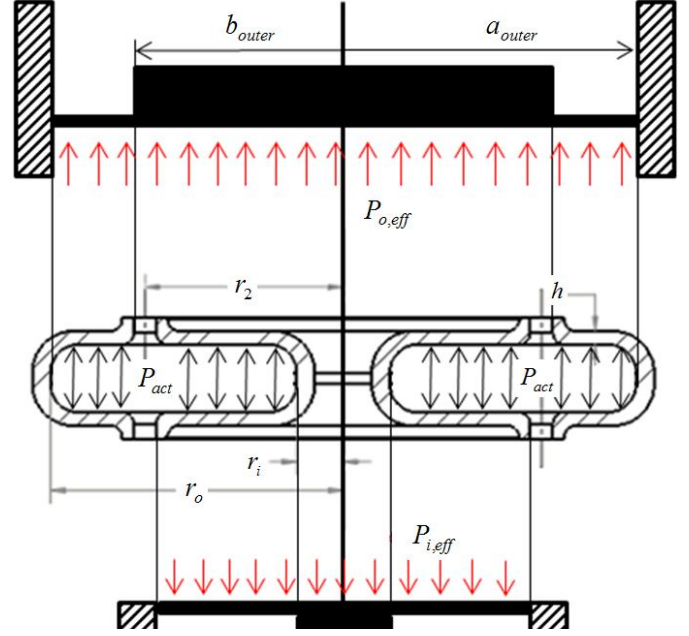


FIG 3. SUPERIMPOSED RIGID-CENTER FLAT DIAPHRAGMS

$$A_p = \frac{3(1-\mu^2)}{16} \left( 1 - \frac{b^4}{a^4} - 4 \frac{b^2}{a^2} \log \frac{a}{b} \right) \quad (10)$$

### Pinching Diaphragm Design

The pinching diaphragm mechanism was designed to grasp the needle without slipping. A short piece of silicone tubing was inserted between the nylon diaphragms and the needle in order to achieve a higher coefficient of friction than the nylon 12. For a flat diaphragm of radius  $a$ , thickness  $h$ , and Young's modulus  $E$ , the maximum deflection occurs at the center and is given by Eq. (11).

$$y_0 = \frac{3(1-\mu^2)}{16} \left( \frac{Pa^4}{Eh^3} \right) \quad (11)$$

The normal force produced for pinching the needle is a result of the difference between the force corresponding to Eq. (11) and the force corresponding to the actual deflection as obstructed by the needle and silicone tubing. Each force can be represented as the product of stiffness and deflection. This normal pinching force is defined by Eq. (12), where  $\Delta y_0$  is the radial interference of the needle and silicone tubing, and a factor of two accounts for the second, opposing diaphragm.

$$F_n = 2 \left( \frac{4\pi Eh^3}{3a^2(1-\mu^2)} \right) \Delta y_0 \quad (12)$$

### Actuator Manufacture

The FFA prototype was manufactured on a 3D Systems Sinterstation 2500 Plus selective laser sintering (SLS) machine

using Nylon 12 powder. To facilitate cleaning out the excess powder from the bellows convolutions and the pinching diaphragms, the design included 20 clean-out holes. Following the clean-out process, Nylon 12 filament was melted to fill and plug each of these holes.

The prototype was designed for use with a needle of outer diameter 2mm, a size consistent with ablation probes currently used for MRI-guided thermal therapy [23]. The current toroidal bellows design can accommodate needle diameters up to 3 mm. Because the FFA can be additively manufactured in a single build, it would require minimal effort to modify the design and produce a prototype to use with higher gauge needles.

The size of a single step on the current prototype is 7 mm and is defined by a mechanical stop which limits the bellows deflection, as shown in Fig. 1. If desired, the step size could be decreased in future design iterations; correspondingly, the bellows displacement vs. pressure characteristic would need to be modified, either by increasing the bellows stiffness or by reducing the number of convolutions on the bellows.

### ACTUATOR CHARACTERIZATION

The system dynamics for the FFA can be approximated by a single acting piston-cylinder with spring return. A free body diagram for the FFA is provided in Fig. 4. Here,  $A$  is the effective cross-sectional area of the bellows,  $b$  the viscous damping of the bellows,  $k$  the bellows spring rate,  $F_f$  the friction between needle and FFA bearing surfaces, and  $F_t$  the tissue reactive forces. The friction and tissue forces exerted on the needle are unknowns that will be addressed later in the formulation of a robust controller. The bellows volume at atmospheric pressure,  $V_{FFA,0}$ , was measured directly from the CAD model.

The spring rate  $k$  is dependent on the stiffness of the nylon bellows and is the summation of the reciprocal of the stiffness of each diaphragm. For diaphragm deflections smaller than  $5h$ , linear deflection and stiffness can be assumed. It is expected that there are slight deviations in linearity as with most deflection characteristics of flat diaphragms. For the prototype

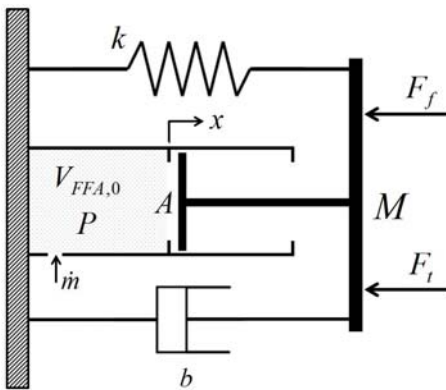


FIG 4. FFA DYNAMIC MODEL

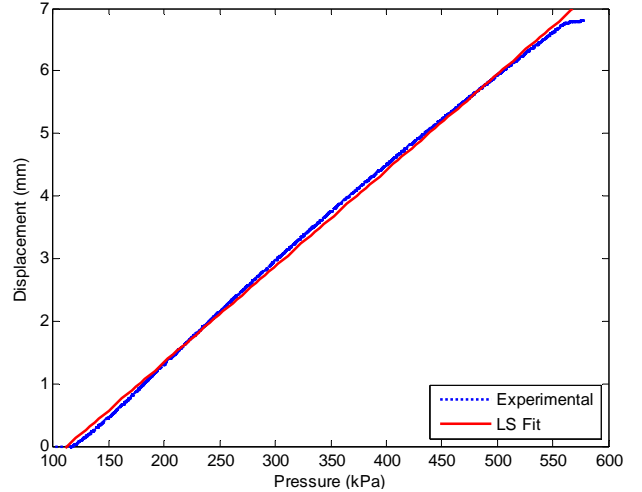


FIG 5. BELLOWS DISPLACEMENT VS. PRESSURE

FFA, the spring rate was experimentally determined by a least-squares linear fit of bellows displacement vs. pressure data, as shown in Fig. 5. This data was obtained by linearly ramping up the bellows pressure from atmospheric pressure to 580 kPa over a duration of two minutes.

The damping coefficient  $b$  is an equivalent viscous damping coefficient dependent upon the loading frequency, and its value was experimentally determined for the FFA prototype. It should be noted that while the FFA dynamic model as presented in Fig. 4 does not include hysteresis effects, the robustness of sliding mode control adequately compensates for this stress dependent viscoelastic behavior. A summary of the actuator characterization is provided in Table 1.

TABLE 1. ACTUATOR PARAMETER VALUES

$E$ , Young's modulus	230 ksi
$\mu$ , Poisson's ratio	0.408
$r_i$ , inner radius of toroid	0.103 in
$r_2$ , convolution connecting ring radius	0.438 in
$b_o$ , $\frac{1}{2}$ thickness of convolutions connector	0.050 in
$r_o$ , outer radius of toroid	0.648 in
$h$ , membrane thickness	0.030 in
$n$ , number of bellows convolutions	5
$A$ , effective cross-sectional bellows area	1.284 in <sup>2</sup>
$k$ , bellows spring rate	308.4 lbf/in
$b$ , bellows damping coefficient	110 lbf-s/in
$M$ , effective mass of bellows & needle	12.4 g
$V_{FFA,0}$ , bellows dead volume	0.996 in <sup>3</sup>

### ACTUATOR PRECISION CONTROL

After fully characterizing the dynamic behavior of the FFA prototype, a nonlinear, model-based controller was developed for precision, sub-step control of needle tip position. This

controller is similar to one developed in prior work for a pneumatically-actuated active cannula robot [20].

### Pressure Dynamics

In this application the pressure dynamics of the pneumatic system are assumed to behave isothermally due to the desired bandwidth. A low bandwidth is suitable and even preferred for image-guided interventions because safety is of paramount concern. Furthermore, bandwidth limitations are also imposed by the long transmission lines that connect the FFA to remotely located, non-MR-compatible valves and pressure transducers. Thus, the pressure dynamics inside the toroidal bellows are well described by Eq. (13)

$$\dot{P} = \frac{RT}{V} \dot{m} - \frac{P\dot{V}}{V} \quad (13)$$

where  $T$  is the ambient temperature,  $R$  the specific ideal gas constant, and  $\dot{m}$  the mass flow into the bellows.

### Valve Mass Flow Dynamics

A proportional spool valve was used to control the mass flow to the bellows. Assuming isentropic flow through a hole in an infinitely thin plate, the area-normalized mass flow  $\Psi$  through the valve orifice is a function of the pressures upstream and downstream of the valve,  $P_u$  and  $P_d$ , respectively, and is described by Eq. (14) [18].

$$\Psi(P_u, P_d) = \begin{cases} \frac{C_1 C_f P_u}{\sqrt{T}} & \text{if } \frac{P_d}{P_u} \leq C_r \text{ (choked)} \\ \frac{C_2 C_f P_u}{\sqrt{T}} \left(\frac{P_d}{P_u}\right)^{1/\gamma} \sqrt{1 - \left(\frac{P_d}{P_u}\right)^{(\gamma-1)/\gamma}} & \text{otherwise (unchoked)} \end{cases} \quad (14)$$

In Eq. (14),  $\gamma = c_p/c_v$  is the ratio of specific heats,  $C_f$  the dimensionless discharge coefficient dependent on orifice geometry, and  $C_r$  the pressure ratio that determines whether the flow is choked or unchoked. For air,  $C_r = 0.5286$ . These constants are calculated using Eqs. (15) and (16), in which  $R$  is the specific ideal gas constant.

$$C_r = \left(\frac{2}{\gamma+1}\right)^{\frac{\gamma}{\gamma-1}} \quad (15)$$

$$C_1 = \sqrt{\frac{\gamma}{R} \left(\frac{2}{\gamma+1}\right)^{(\gamma+1)/(\gamma-1)}} \quad \text{and} \quad C_2 = \sqrt{\frac{2\gamma}{R(\gamma-1)}} \quad (16)$$

The mass flow is simply the product of valve orifice area  $A_v$  and area-normalized mass flow, as given by Eqs. (17) and (18). When the signed valve orifice area is positive, mass flow is positive and the bellows is charging. When the signed valve

orifice area is negative, mass flow is negative and the bellows is exhausting. In Eq. (18), the supply pressure and atmospheric pressure are denoted  $P_s$  and  $P_{am}$ , respectively.

$$\dot{m} = A_v \Psi(P_u, P_d) \quad (17)$$

$$\Psi(P_u, P_d) = \begin{cases} \Psi(P_s, P) & \text{for } A_v \geq 0 \\ \Psi(P, P_{am}) & \text{for } A_v < 0 \end{cases} \quad (18)$$

### Equation of Motion

Referring to Fig. 4, the equation of motion for the FFA is given by

$$M\ddot{x} = (P - P_{am})A - b\dot{x} - kx - F_f - F_t \quad (19)$$

For implementing pneumatic servo control with a mass flow proportional valve, Eq. (19) is differentiated with respect to time such that the control variable, namely the valve orifice area  $A_v$ , appears by substituting in the pressure and mass flow dynamics from Eqs. (13) to (18). The result, expressed in companion form, is given by Eq. (20).

$$\ddot{x} = f(P, V, \dot{x}, \ddot{x}) + g(V, P_u, P_d)A_v \quad (20)$$

In Eq. (20),  $f(\cdot)$  and  $g(\cdot)$  are nonlinear functions of the states and are given Eqs. (21) and (22).

$$f(P, V, \dot{x}, \ddot{x}) = -\frac{1}{M} \left( \frac{PA^2}{V} + k \right) \dot{x} - \frac{b}{M} \ddot{x} - \frac{1}{M} (\dot{F}_f + \dot{F}_t) \quad (21)$$

$$g(V, P_u, P_d) = \frac{A}{M} \frac{RT}{V} \Psi(P_u, P_d) \quad (22)$$

### Sliding Mode Controller

Due to unknown forces in the system, namely friction and tissue reactive forces, a robust controller was needed. For similar experimental setups in prior work, the authors have had good success with sliding mode control (SMC), as this approach is well-suited for highly nonlinear plants like the pneumatic servo [19, 20] (see [24] for a primer on SMC). Removing the unknowns  $F_f$  and  $F_t$  from Eq. (19), a known approximation for the plant is given by Eqs. (23) and (24).

$$\ddot{x} = \hat{f}(P, V, \dot{x}, \ddot{x}) + g(V, P_u, P_d)A_v \quad (23)$$

$$\hat{f}(P, V, \dot{x}, \ddot{x}) = -\frac{1}{M} \left( \frac{PA^2}{V} + k \right) \dot{x} - \frac{b}{M} \ddot{x} \quad (24)$$

A sliding surface third order in position was formulated as described by Eq. (25). It includes integral action to eliminate steady-state error, and the desired location for the closed-loop

poles is  $-\lambda$ . By conventional SMC theory the position error is defined as  $e = x - x_d$ , where the desired position is  $x_d$ .

$$s = \left( \frac{d}{dt} + \lambda \right)^3 \int e \quad (25)$$

It is desired to force the  $s$  dynamics and hence the error to smoothly decay to zero. This behavior is ensured to occur if the time derivative  $\dot{\mathcal{V}}$  of the Lyapunov function  $\mathcal{V} = \frac{1}{2}s^2$  can be made negative definite. A negative definite function was chosen as described by Eqs. (26) and (27).

$$\dot{\mathcal{V}} = s\dot{s} \leq -\eta s \text{sat}(s/\phi) \quad (26)$$

$$\text{sat}(s/\phi) = \begin{cases} -1 & s < -\phi \\ s/\phi & -\phi \leq s \leq \phi \\ +1 & s > \phi \end{cases} \quad (27)$$

In Eq. (26),  $\eta$  is the positive constant for robustness and  $\phi$  the boundary layer for reducing chatter.

A control law satisfying the behavior described by Eq. (26) is obtained by taking the time derivative of Eq. (25) and plugging in Eq. (23). Then the result, Eq. (28), is set equal to the right hand side of Eq. (26). After rearranging, an expression for the control variable  $A_v$  is obtained, and this control law is given by Eq. (29).

$$\dot{s} = \hat{f}(P, V, \dot{x}, \ddot{x}) + g(V, P_u, P_d)A_v - \ddot{x}_d + 3\lambda\ddot{e} + 3\lambda^2\dot{e} + \lambda^3e \quad (28)$$

$$A_v = k_p \frac{\ddot{x}_d - \hat{f}(P, V, \dot{x}, \ddot{x}) - 3\lambda\ddot{e} - 3\lambda^2\dot{e} - \lambda^3e - \eta \text{sat}(s/\phi)}{g(V, P_u, P_d)} \quad (29)$$

During initial experimental testing of the control law, it was observed that the controller was overpowered. A proportional gain  $k_p$  was thus introduced to scale down the magnitude of the valve command. A summary of the pneumatic servo controller parameters is provided in Table 2.

TABLE 2. PNEUMATIC SERVO CONTROL PARAMETERS

$C_f$	0.2939
$C_r$	0.5826
$\eta$	2 m/s <sup>3</sup>
$\lambda$	120 Hz
$\phi$	1 m/s <sup>2</sup>
$k_p$	0.1

## EXPERIMENTAL SETUP

As a first test for proper functionality of the FFA, the FFA was connected to two valves (Enfield LS-V05s), one for charging and exhausting the toroidal bellows and a second valve for charging and exhausting the pinching diaphragm mechanism. Using National Instruments LabView and an NI-USB6211 and NI-cDAQ-9178 for data acquisition, the valves were commanded to charge and exhaust according to the two sequences previously described for advancement and retraction of the needle. The FFA successfully translated the needle over multiple steps in both directions.

A second experimental setup was constructed as shown in Fig. 1 for evaluating the sub-step positioning control of the sliding mode controller. Here, an optical linear encoder (US Digital EM1-0-500-I) was mounted to the stationary housing surrounding the toroidal bellows. A transmissive strip with a digital scale of 500 lines per inch (US Digital LIN-500-1-N) was mounted to the moving end of the bellows. Two 5-port/4-way valves (Festo MPYE-5-M5-010-B) were used, with a plug on one output port of each valve. Two pressure transducers (Festo SPTW-P10R-G14-VD-M12) were used to measure pressure upstream and downstream of the control valve for the bellows. For data acquisition, a National Instruments NI-6229 PCI card was used with MATLAB Simulink and xPC Target.

Pneumatic transmission lines 3.5 meters long connected the FFA to the valves, and a long double-shielded IEEE 1394 cable connected the optical encoder to the controller electronics. These long lines and cables are being used because in future experiments, the FFA will be placed inside the MRI scanner, while the non-MR-compatible valves and electronics will need to be remotely located.

## EXPERIMENTAL RESULTS

The sliding mode controller was tested for tracking positions within the step size range of the FFA. The commanded position was a square-like wave of frequency 0.0625 Hz, with smooth corners. Using a slew rate limit of  $\pm 16$  mm/sec, the sharp corners of the square wave were removed so as to eliminate overshoot that was observed during initial testing.

The results for one 80-second run are shown in Fig. 6. A bellows position of 0 mm corresponds to the bellows uncharged at atmospheric pressure. During this run, the FFA was held vertically, such that the motion of the needle and effective mass of the bellows were subject to an opposing gravitational force. Thus, these results demonstrate that the controller successfully positions the needle when the FFA has been rotated to various orientations. The mean and maximum steady-state errors in Fig. 4 are 0.025 and 0.044 mm, respectively.

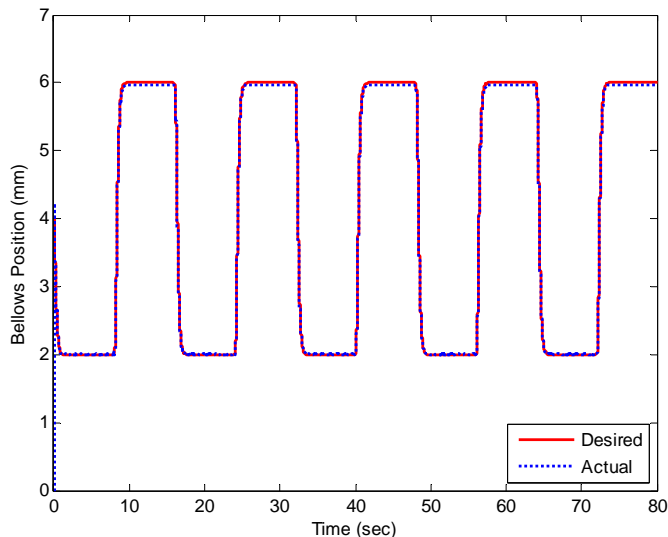


FIG 6. FFA PRECISION POSITION TRACKING

Due to hysteresis effects, relaxation of the bellows was observed to occur after the initial response to a change in commanded position. This behavior is evident by looking at the bellows pressure vs. time during position tracking of the square-like wave, as shown in Fig. 7. After the bellows has extended to a position of 6 mm, the material relaxes and less pressure is required to maintain the bellows at this position. This explains the pressure decays along the top of the plotted data in Fig. 7. Similarly, along the bottom of the plotted data in Fig. 7, the gradual increase in pressure is caused by the loss of strain energy as the bellows contracts.

## CONCLUSIONS

Magnetic resonance imaging (MRI) offers many benefits to image-guided interventions, as it provides a variety of contrast

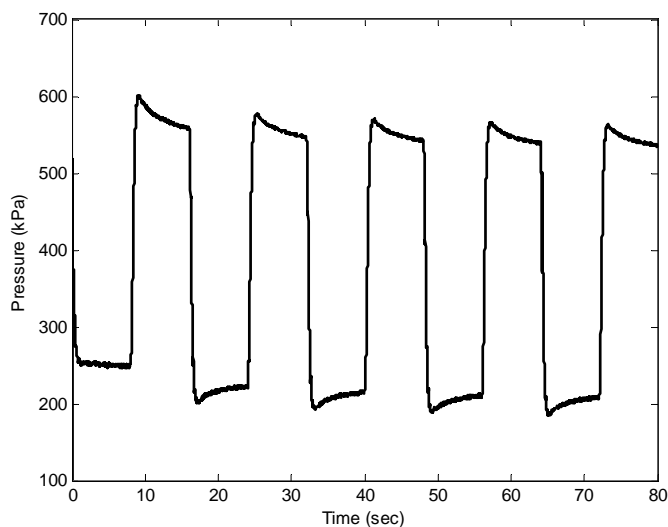


FIG 7. BELLOWS PRESSURE VS TIME

mechanisms for excellent soft tissue distinction and therapy monitoring (e.g. MR perfusion, thermometry). Its capabilities for on-the-fly adjustment of imaging planes and volumes can reduce repositioning of patient or imager, and MRI does not expose clinician or patient to ionizing radiation [8]. Due to the tight confines and strong magnetic field of closed-bore MR scanners, robots employing compact, non-magnetic, low-noise actuators are needed for access to the patient in many cases of in-scanner interventions.

This paper has reported work towards the development of such an actuator. The prototype flexible fluidic actuator (FFA) was designed to be compact, sterilizable and inherently safe, using a linear stepper mechanism with hermetically sealed bellows and needle grasper. Manufactured in a single build on a selective laser sintering (SLS) machine, the actuator was fully characterized, and the results validated the analytical model. In initial experiments for sub-step control, a nonlinear, model-based controller achieved a mean steady-state positioning accuracy of 0.025 mm. These promising results will be built upon in future experiments for positioning the needle tip using image guidance.

## REFERENCES

- [1] Stoianovici, D., Patriciu, A., Petrisor, D., Mazilu, D., and Kavoussi, L., 2007. "A New Type of Motor: Pneumatic Step Motor," *IEEE/ASME Trans Mechatronics*, **12**(1):98-106.
- [2] Muntener, M., Patriciu, A., Petrisor, D., Schär, M., Ursu, D., Song, D. Y., and Stoianovici, D., 2008. "Transperineal Prostate Intervention: Robot for Fully Automated MR Imaging—System Description and Proof of Principle in a Canine Model," *Radiology*, **247**(2):543-549.
- [3] Zemitte, N., Bricault, I., Fouard, C., Sanchez, B., and Cinquin, P., 2008, "LPR: A CT and MR-Compatible Puncture Robot to Enhance Accuracy and Safety of Image-Guided Interventions," *IEEE/ASME Trans Mechatronics*, **13**(3):306-315.
- [4] Van den Bosch, M. R., Moman, M. R., van Vulpen, M., Battermann, J. J., Duiveman, E., van Schelven, L. J., de Leeuw, H., Lagendijk, J. J. W., and Moerland, M. A., 2010. "MRI-guided robotic system for transperineal prostate interventions: proof of principle," *Phys Med Biol*, **55**:133-140.
- [5] Melzer, A., Gutmann, B., Remmele, T., Wolf, R., Lukoscheck, A., Bock, M., Bardenheuer, H., and Fischer, H., 2008. "INNOMOTION for Percutaneous Image-Guided Interventions: Principles and Evaluation of this MR- and CT-Compatible Robotic System," *IEEE Eng Med Biol Mag*, May/June, pp. 66-73.
- [6] Tokuda, J., Song, S., Fischer, G. S., Iordachita, I. I., Seifabadi, R., Cho, N., Tuncali, K., Fichtinger, G., Tempany, C., and Hata, N., 2012. "Preclinical evaluation of an MRI-compatible pneumatic robot for angulated needle placement in transperineal prostate interventions," *Int J CARS*, **7**:949-957.

- [7] Masamune, K., Kobayashi, E., Masutani, Y., Suzuki, M., Dohi, T., Iseki, H., and Takakura, K., 1995. "Development of an MRI-Compatible Needle Insertion Manipulator for Stereotactic Neurosurgery," *J Image Guid Surg*, **1**:242-248.
- [8] Tsekos, N., Khanicheh, A., Christoforou, E., and Mavroidis, C., 2007. "Magnetic Resonance-Compatible Robotic and Mechatronics Systems for Image-Guided Interventions and Rehabilitation: A Review Study," *Annu Rev Biomed Eng*, **9**:351-387.
- [9] Sutherland, G., Latour, I., Greer, A. D., Fielding, T., Feil, G., and Newhook, P., 2008. "An Image-Guided Magnetic Resonance-Compatible Surgical Robot". *Neurosurgery*, **62**(2):286-293.
- [10] Su, H., Cardona, D. C., Shang, W., Camilo, A., Cole, G. A., Rucker, D. C., Webster III, R. J., and Fischer, G. S., 2012. "A MRI-Guided Concentric Tube Continuum Robot with Piezoelectric Actuation: A Feasibility Study," *IEEE International Conference on Robotics and Automation*, pp. 1939-1945.
- [11] Proulx, S. and Plante, J., 2011. "Design and Experimental Assessment of an Elastically Averaged Binary Manipulator Using Pneumatic Air Muscles for Magnetic Resonance Imaging Guided Prostate Interventions," *J Mech Des*, **133**(11):1-9.
- [12] Ikuta, K., Hironobu, I., Katsuya, S., and Takahiro, Y., 2003. "Micro Hydrodynamic Actuated Multiple Segments Catheter for Safety Minimally Invasive Therapy," *Proc IEEE Int Conf Robot Automat*, pp. 2640-2645.
- [13] Haga, Y., Matsunaga, T., Makishi, W., Totsu, K., Mineta, T., and Esashi, M., 2006. "Minimally Invasive Diagnostics and Treatment using Micro/Nano Machining," *Minimally Invasive Therapy*, **15**(4):218-225.
- [14] De Greef, A., Lambert, P., and Delchambre, A., 2009. "Towards Flexible Medical Instruments: Review of Flexible Fluidic Actuators," *Precision Engineering*, **33**(4):311-321.
- [15] Reynolds, D. B., Repperger, D. W., Phillips, C. A., and Bandy, G., 2003. "Modeling the Dynamic Characteristics of Pneumatic Muscle," *Ann Biomed Eng*, **31**(3):310-317.
- [16] Slightam, J. E. and Gervasi, V. R., 2012. "Novel Integrated Fluid-Power Actuators for Functional End-Use Components and Systems via Selective Laser Sintering Nylon 12," *23<sup>rd</sup> Ann Int Solid Freeform Fabrication Symp*, Austin, TX, pp. 197-211.
- [17] Richer, E. and Hurmuzlu, Y., 2000. "A High Performance Pneumatic Force Actuator System: Part I—Nonlinear Mathematical Model," *ASME J Dyn Syst, Meas Control*, **122**(3):416-425.
- [18] Richer, E. and Hurmuzlu, Y., 2000. "A High Performance Pneumatic Force Actuator System: Part II—Nonlinear Controller Design," *ASME J Dyn Syst, Meas Control*, **122**(3):426-434.
- [19] Zhu, Y., and Barth, E. J., 2010. "Accurate Sub-Millimeter Servo-Pneumatic Tracking using Model Reference Adaptive Control (MRAC)," *Int J Fluid Power*, **11**(2):49-57.
- [20] Comber, D. B., Barth, E. J., and Webster III, R. J., 2013. "Design and Control of an MR-Compatible Precision Pneumatic Active Cannula Robot," *ASME J Med Devices*, [In Press].
- [21] Comber, D. B., Webster III, R. J., Neimat, J. S., and Barth, E. J., 2013. "Open-Loop Tip Accuracy of an MRI-Compatible Active Cannula Robot," *Proc Hamlyn Symp Medical Robotics*, London, pp. 112-113.
- [22] Di Giovanni, M., 1982, *Flat and Corrugated Diaphragm Design Handbook*, Marcel Dekker, New York, pp. 130-192.
- [23] Curry, D. J., Gowda, A., McNichols, R. J., and Wilfong, A. A., 2012. "MR-Guided Stereotactic Ablation of Epileptogenic Foci in Children," *Epilepsy and Behavior*, **24**(4):408-414.
- [24] Slotine, J. E. and Li, W., *Applied Nonlinear Control*, pp. 276-301, Prentice Hall, 1991.